

Silicon nitride-based Kerr frequency combs and applications in metrology

Zhaoyang Sun,^a Yang Li,^{a,*} Benfeng Bai,^{a,*} Zhendong Zhu,^b and Hongbo Sun^{a,*}

^aTsinghua University, State Key Laboratory of Precision Measurement and Instruments, Department of Precision Instrument, Beijing, China

^bNational Institute of Metrology, Beijing, China

Abstract. Kerr frequency combs have been attracting significant interest due to their rich physics and broad applications in metrology, microwave photonics, and telecommunications. In this review, we first introduce the fundamental physics, master equations, simulation methods, and dynamic process of Kerr frequency combs. We then analyze the most promising material platform for realizing Kerr frequency combs—silicon nitride on insulator (SNOI) in comparison with other material platforms. Moreover, we discuss the fabrication methods, process optimization as well as tuning and measurement schemes of SNOI-based Kerr frequency combs. Furthermore, we highlight several emerging applications of Kerr frequency combs in metrology, including spectroscopy, ranging, and timing. Finally, we summarize this review and envision the future development of chip-scale Kerr frequency combs from the viewpoint of theory, material platforms, and tuning methods.

Keywords: Kerr frequency comb; silicon nitride; Lgiato–Lefever equation; damascene process; precision measurements.

Received Aug. 7, 2022; revised manuscript received Oct. 17, 2022; accepted for publication Oct. 20, 2022; published online Nov. 14, 2022.

© The Authors. Published by SPIE and CLP under a Creative Commons Attribution 4.0 International License. Distribution or reproduction of this work in whole or in part requires full attribution of the original publication, including its DOI.

[DOI: [10.1117/1.AP.4.6.064001](https://doi.org/10.1117/1.AP.4.6.064001)]

1 Introduction

As one of the most fundamental technologies, metrology has been widely used in daily life, defense, healthcare, astronomy, and fundamental science. Conventional metrology methods such as atomic clocks usually involve complicated and bulky systems for a particular measurement target. Utilizations of frequency combs in metrology enable simple, compact, and multifunctional instruments. Figure 1 shows applications of microcombs in ultrafast ranging, astronomical spectrograph calibration, spectroscopy, timing, communications, and ultralow noise frequency synthesis.^{1–6} Frequency combs refer to a series of equally spaced spectral lines in the frequency domain, corresponding to a series of equally spaced pulses in the time domain. Kerr frequency combs can be described by the comb equation with the help of the Fourier series:⁷

$$E(t) = A(t)e^{i\omega t} = \sum_{N=N_i}^{N_j} A_N e^{i\omega_N t}, \quad (1)$$

where ω_N is the angular frequency of one of the modes in the comb pulses and N is the mode number corresponding to ω_N . Assuming the radius of the microresonator is R , the round-trip time is $\tau = \frac{2\pi n_g R}{c}$, where n_g is the group index. In the comb generation process, it is ideal to achieve a steady state, such as a single soliton state, in which there is only one pulse in a round trip and there is only one pulse coupling out in one round trip. Hence, the time interval of the impulse sequence coupling out of the resonator is equal to the round-trip time, corresponding to the repetition rate $f_r = \frac{1}{\tau} = \frac{c}{2\pi n_g R}$. The repetition rate is equal to the free spectral range (FSR) of the microresonator. However, the frequency of the cavity modes is not necessary for the integer times of f_r . To lock the cavity modes, we also need the offset frequency f_0 to determine the cavity mode frequency f_N :

$$f_N = f_0 + Nf_r, \quad (2)$$

which is the comb equation and $f_N = \frac{\omega_N}{2\pi}$, where ω_N is the angular frequency in Eq. (1). Additionally, f_0 is related to the carrier-envelope offset phase φ_{ceo} , which is used to characterize the phase locking:

*Address all correspondence to Yang Li, yli9003@mail.tsinghua.edu.cn; Benfeng Bai, baibenfeng@tsinghua.edu.cn; Hongbo Sun, hbsun@tsinghua.edu.cn

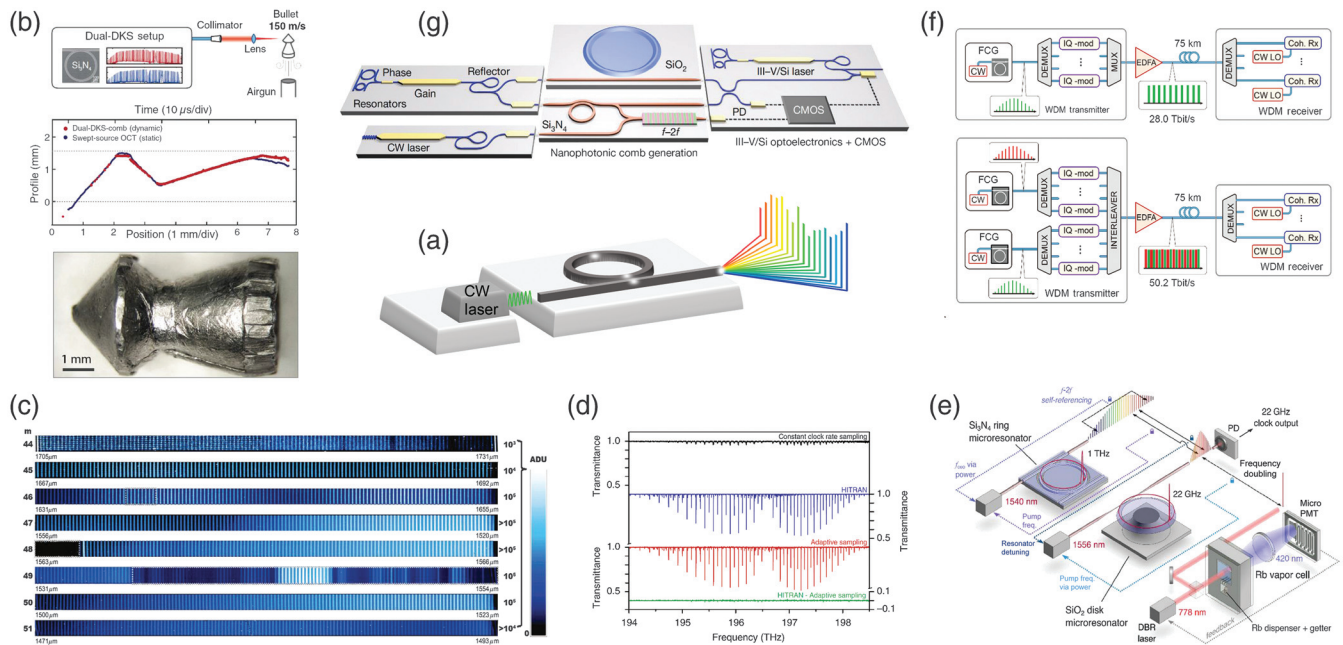


Fig. 1 Chip-scale frequency comb and its applications. (a) Under a continuous wave (CW) pump, a microring resonator generates a Kerr frequency comb. (b) Dual-comb for ultrafast ranging. © 2018 American Association for the Advancement of Science (AAAS). (c) Kerr frequency comb for astronomical spectrograph calibration. © 2019 Nature Publishing Group. (d) Dual-comb spectroscopy. © 2014 Nature Publishing Group. (e) Two interlocked combs for timing. © 2019 Optica Publishing Group. (f) Frequency combs for communications. © 2017 Nature Publishing Group. (g) Frequency combs for ultralow noise frequency synthesis. © 2018 Nature Publishing Group. Reproduced with permission.¹⁻⁶

$$f_0 = \frac{1}{2\pi} \frac{d\varphi_{\text{ceo}}}{dt}. \quad (3)$$

This basic knowledge is applicable to all types of Kerr frequency combs including mode-locked lasers, fiber-based frequency combs, and microcavity-based frequency combs.

In recent years, the fast development of chip-scale frequency combs leads to the miniaturization of metrology instruments. Among these dissipative Kerr frequency combs stand out because its soliton states have an ultralow phase noise.⁸ For example, microcomb-based microwave synthesis can realize a much lower noise level than that based on a Brillouin oscillator.^{9,10} The combs' nonlinear dynamic evolution and stabilization process can be well described by the Lgiato-Lefever equation (LLE).¹¹ Moreover, mode-crossing induced spectrum jump and broadening can help us in designing better cavities.^{12,13} The development of material platforms and fabrication techniques facilitates a low-power pump.^{14,15} Arising new tuning methods enables us to simply access the soliton states.¹⁶ Chip-scale turnkey soliton combs pumped by a DFB laser were achieved recently,¹⁷ paving the avenue of integrating various metrology instruments in a cellphone chip.

This review is organized as follows. Section 2 focuses on the underlying physics and LLE-based simulations of Kerr frequency combs. Section 3 introduces the material platforms and fabrication techniques. The Damascene process is emphasized because it dramatically reduces losses and cracks induced by stress. Section 4 presents the measurement setups and tuning

methods. To access the soliton states easily, the dynamic tuning process in balancing the thermal effect and the nonlinearity is introduced in detail. Section 5 illustrates the applications of Kerr frequency combs in spectroscopy, ranging, and timing. Finally, we summarize this review and envision the future development of silicon nitride-based Kerr frequency combs.

2 Theory

A frequency comb is a series of equidistant discrete spectral lines in the frequency domain, corresponding to a train of pulses in the time domain. It can be well described and predicted by the LLE, which was proposed in 1987¹⁸ to describe the pattern formation in nonlinear optics. After 20 years, Del'Haye et al.¹⁹ demonstrated the first Kerr frequency comb using a continuous wave (CW) pump in a silica toroidal microcavity. In 2016, Brasch et al.¹⁵ realized two-third of an octave by using soliton-induced Cherenkov radiation, and in the following year, Li et al.²⁰ achieved octave-spanning combs on the silicon nitride platform. At present, microresonators are attracting a lot of interest in the community of frequency combs. Along with the development of microresonator-based frequency combs, LLE evolved from the original form to the common style,^{11,21-27} becoming a powerful tool to describe and predict the light-microresonator interaction. This section first briefly introduces the generation of frequency combs from the physical point of view. Then, the mathematical description and solutions are given. Finally, an example is given to interpret how to couple a system's unneglectable side effects with LLE.

2.1 Generation of Combs

The response of a material to the applied light wave can be characterized by the dielectric tensor when the magnetic response is neglectable. In the dielectric tensor, each element ϵ_{ij} represents the effect of the electric field in the i direction on the material in the j direction. If ϵ_{ij} is a complex number, its imaginary part represents the gain or loss of the material. Furthermore, the higher-order nonlinear tensors can be added to consider the nonlinear response of the material to in turn better model the interaction process.

Any electromagnetic phenomenon is governed by Maxwell equations. If we neglect the magnetic response, an applied harmonic electrical field induces the polarization of the material in which the electric dipoles are aligned with the direction of the applied electric field. Because different materials have different intrinsic oscillation frequencies, dipoles cannot follow the applied electrical field at all frequencies, leading to dispersion. Therefore, the elements in the dielectric tensor $\epsilon(\omega)_{ij}$ are eigen functions of frequency. Because the polarization process induces both linear and nonlinear responses, the polarization can be expanded according to the Taylor series, leading to the nonlinear polarization tensor.

The nonlinear polarization term can be treated as a perturbation due to the fact that the nonlinear coefficient is much smaller than the linear coefficient. Because polarization is the eigen function in the frequency domain, the effect of polarization can be expressed in epsilon in the form of $\epsilon(\mathbf{r}, \omega, \|\mathbf{E}\|^2)$. Using the model expansion approach and normalization condition, we can derive the coupled mode equations from the passive Maxwell equations:^{25,28,29}

$$\frac{\partial a_\mu}{\partial \tau} = -(1 + i\zeta_\mu)a_\mu + i \sum_{\mu' < \mu} (2 - \delta_{\mu'\mu'}) a_{\mu'} a_{\mu''} a_{\mu'+\mu''-\mu}^* + \delta_{0\mu} f, \quad (4)$$

where a_μ is the normalized slowly varying amplitude of the mode at ω_μ , f is the normalized pump power, and ζ_μ is the detuning factor. This coupled mode equation can be the governing equation for the Kerr frequency comb generation process with several modes.³⁰ Although it is difficult to solve this equation analytically, the numerical simulations can provide satisfactory solutions, showing a good agreement with the experimental results. Numerical simulations can give solutions to the threshold problem and generation of primary combs. However, because the computation time increases cubically with the number of modes,²⁹ the numerical simulation is not efficient in dealing with a large number of modes interacting with each other.

From the viewpoint of physics, the comb generation requires the balance between nonlinearity and dispersion as well as the balance between gain and loss.³¹ The nonlinearity gives rise to all the comb lines except the pump while the dispersion limits the span of the comb spectrum. From the engineering point of view, we need a microcavity whose internal boundary can induce constructive interference of multiple round trips of light. This cavity's geometry can be a sphere, a cylinder, a toroid, a wedge, a disk, a ring, or any other circular shape. Then, we need to couple a pump light into the microcavity and couple out the generated comb. Usually, evanescent coupling is achieved with a prism,^{32,33} fiber,^{34,35} and waveguide.^{36,37} To achieve critical coupling, we need to optimize the structural parameters.³⁸ Inside the microresonator, we need to satisfy the conditions of phase matching and low loss. The total losses Q_{tot} include material

loss, scattering loss, and coupling loss. Once the intracavity power exceeds a certain threshold, we can observe the nonlinear response. The conservation of energy and momentum of a Kerr nonlinear process can be expressed as

$$\hbar\omega_1 + \hbar\omega_2 = \hbar\omega_3 + \hbar\omega_4, \quad (5)$$

$$\hbar\mathbf{k}_1 + \hbar\mathbf{k}_2 = \hbar\mathbf{k}_3 + \hbar\mathbf{k}_4. \quad (6)$$

Due to the dispersion, it is challenging to achieve the conservations of both energy and momentum simultaneously over the entire comb spectrum. For the resonant modes of the microcavity, the conservation of momentum is always satisfied.³⁹

$$m\lambda = 2\pi Rn(\lambda), \quad (7)$$

$$k = \frac{2\pi n(\lambda)}{\lambda} = \frac{m}{R}. \quad (8)$$

As long as the mode number satisfies $n + m = q + p$, the momentum is conserved. On the other hand, the mode frequency

$$\omega = \frac{2\pi c}{\lambda} = \frac{mc}{n(\lambda)R} \quad (9)$$

is determined by the dispersion, the thermal effect $n(\lambda, T)$, and the nonlinear refractive index $n = n_0 + n_2 I$. Considering all these effects, the comb lines are not exactly equally spaced. Without considering the high-order dispersion terms, it is reasonable to approximate all the comb lines with an equal spacing using the perturbation approximation.

After the satisfaction of the following conditions: light coupling to the resonant mode of the cavity, the intracavity power exceeding the threshold, and the phase matching condition, nonlinear effects govern the physical process with dispersion, leading to the degenerate four-wave mixing (FWM) process. In this process, two photons with the same frequency ω_0 transfer to another two photons with different frequencies ω_1 and ω_2 , satisfying $2\omega_0 = \omega_1 + \omega_2$ (Fig. 2). Here, ω_0 is the pump frequency while the seed frequencies ω_1 and ω_2 are determined by the vacuum fluctuation. FWM results in the redistribution of energy from the pump mode to the two primary sidemodes. When this process reaches a certain threshold, the cascaded FWM process appears. In this process, any two of the pump mode and two sidemodes with frequencies ω_m and ω_n transfer to another two modes with frequencies ω_p and ω_q , satisfying $\omega_m + \omega_n = \omega_p + \omega_q$ in which the frequencies ω_p and ω_q are determined by the vacuum fluctuation. This process cascades until reaching an equilibrium state, generating all the resonant modes of the cavity—the comb lines. For non-resonant modes, even if they are generated by the cascaded FWM process, they will disappear quickly because of the phase mismatching.

The microcavity-based Kerr frequency combs require the anomalous dispersion to broaden the comb spectrum range, which is limited by the contraction of pulses due to nonlinearity. In a microcavity, dispersion of the waveguide is determined not only by the material dispersion but also by the mode dispersion, coupling dispersion, and bending dispersion. An ideal material for microcavity-based Kerr frequency combs needs to meet the

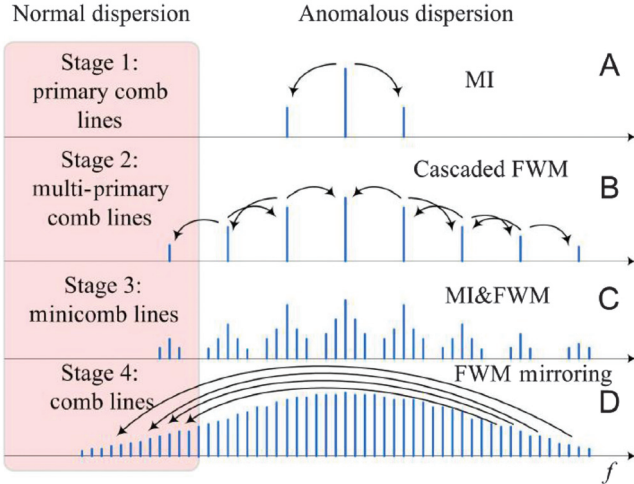


Fig. 2 The generation process of Kerr frequency combs. When the pump power couples into the resonator, the primary comb lines arise by MI first. Along the tuning process, cascaded FWM is generated, resulting in more comb lines. Finally, the comb is formed after further tuning. © 2016 De Gruyter. Reproduced with permission.⁴⁰

following conditions. First, the material needs to show low absorption losses in the comb spectrum to achieve an ultrahigh Q . Second, the material's laser damage threshold needs to be higher than the threshold for generating the Kerr frequency comb. Third, the material needs to show anomalous dispersion in the comb spectral regime. With such a material, an ultrahigh Q can be achieved by improving the manufacturing techniques. We usually select inorganic materials to provide a higher laser damage threshold. Furthermore, the flat dispersion regime of the material can be used to achieve anomalous modal dispersion via structural engineering of the waveguide,^{41,42} increasing the total anomalous dispersion regime of the waveguide. Figure 3 illustrates the dispersion engineering with different parameters. Through structural optimization, the anomalous dispersion range can be broadened. Moreover, when high-order dispersion engineering is introduced, an octave comb can even be achieved.

Normal dispersion can also support the Kerr comb generation. Compared with anomalous dispersion, normal dispersion can only support dark solitons with the opposite chirp to balance the dispersion and nonlinearity. In the dark soliton case, the combs are related to interlocked switching waves between two homogeneous states.⁴⁴ Recently, normal dispersion combs were used in soliton spectrum broadening via cross-phase modulation.⁴⁵ Compared with combs generated in the anomalous dispersion regime, the comb existing area is much smaller in the normal dispersion regime (Fig. 4).

This review focuses on the anomalous dispersion case, in which the comb spectra only appear in the anomalous region. To obtain a broader spectrum, a wider anomalous dispersion region is desired. For a given material, we can engineer the geometric parameters of the waveguide's cross section to achieve the desired anomalous modal dispersion. Additionally, the total dispersion can be further adjusted by engineering the ring curvature, coupling distance, and crossing between different modes.

2.2 LLE and Solutions

Although coupled wave equations can predict the experimental results via numerical simulations using an adaptive stepsize Runge–Kutta integrator, the efficiency is not very high, especially for multimode cases. On the other hand, LLE can describe Kerr frequency combs. Chembo et al.¹¹ demonstrated that coupled wave equations are equivalent to a variant of LLE. Compared with coupled wave equations, LLE has a more concise formalization and a faster solving speed because of utilizing a split-step Fourier transform (SSFT). It was first proposed by Lugiato and Lefever¹⁸ to describe the spontaneously formed stationary spatial dissipative structure in the nonlinear optical field, just like Turing patterns in zoology.⁴⁷ After over 30 years of development, LLE can be presented in the form of a driven, detuned, and damped nonlinear Schrödinger equation (NLS).⁴⁸ The typical LLE for Kerr frequency combs is^{11,24,49}

$$\frac{\partial E}{\partial t} = -(1 + i\alpha)E + i|E|^2E - i\frac{\beta}{2}\frac{\partial^2 E}{\partial \theta^2} + F. \quad (10)$$

In this expression, E is the normalized intracavity field envelope; F is the normalized input field amplitude; the azimuth angular variable θ is defined as $\theta = \frac{z}{R} \in (-\pi, \pi]$, where R is the radius of the cavity, z is propagation direction along which there is a periodic boundary condition; α is the detuning parameter and can be expressed as $\alpha = -2Q_0\frac{\Omega_0 - \omega_0}{\omega_0}$, where Q_0 is the loaded quality factor for mode frequency ω_0 , Ω_0 is the input field frequency, and ω_0 is the resonant mode frequency the closest to Ω_0 ; β is the dispersion parameter and can be expressed as $\beta = \frac{2Q_0c}{\omega_0 R^2} \frac{\partial v_g}{\partial \omega} |_{\omega=\omega_0}$, where v_g is the group velocity and c is the speed of light in a vacuum. All the amplitude terms can be interpreted as photon numbers after normalization with respect to $\hbar\omega$. LLE's analytical solution is available in the case of zero dispersion⁵⁰ and an approximate solution can be found by using the Lagrangian perturbation approach.^{51,52} Solving LLE numerically by using an FFT can give an accurate solution with an efficiency much higher than that of solving coupled mode equations by using an R–K integral.

To numerically solve Eq. (13), we define the differential operator \hat{D} and nonlinear operator \hat{N} :

$$\hat{D} = -\left(1 + i\frac{\beta}{2}\frac{\partial^2}{\partial \theta^2}\right), \quad (11)$$

$$\hat{N} = i|E|^2 - i\alpha. \quad (12)$$

Combining with the split-step Fourier method and R–K integration, we can easily derive⁵³

$$E(T, \theta) = \left\{ FT^{-1} \left[\tilde{E}(t_0) e^{\frac{1}{2}\hat{D}T} \right] + \frac{\hbar}{2} F \right\} e^{\frac{\hbar}{2}\hat{N}T}. \quad (13)$$

With such a solution, we can simulate the physical process in both dynamic and stable states and in turn tune the parameters to optimize the results.^{11,26,46}

In addition to the numerical simulation, an analytical soliton solution can also be derived from LLE. Treating the pump and dissipation as perturbations, via the Lagrangian variation

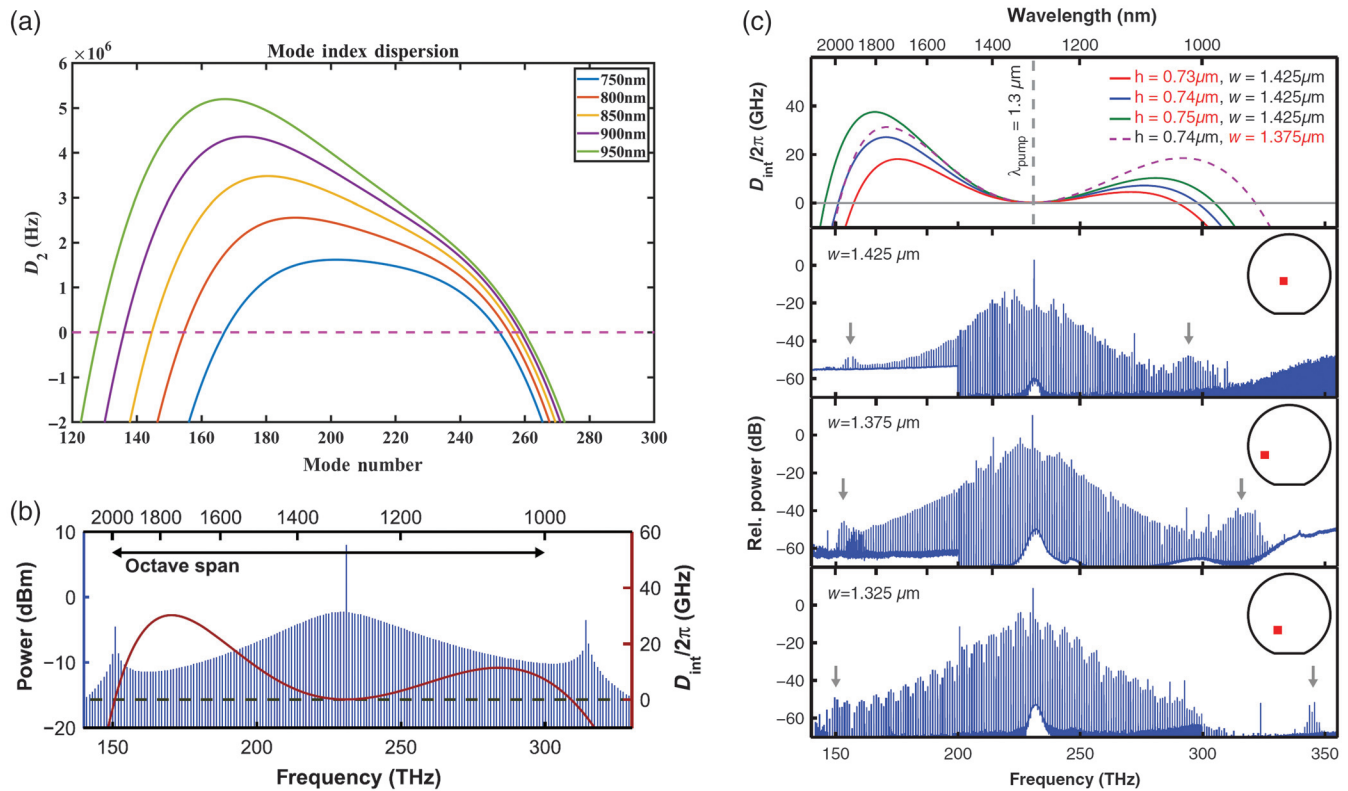


Fig. 3 Dispersion engineering broadens the comb spectrum. (a) The anomalous dispersion regimes correspond to waveguides with different cross-section dimensions. (b) Dispersive waves induce spectrum broadening. (c) Dispersive waves of waveguides with different cross-section dimensions. © 2017 Optica Publishing Group. Reproduced with permission.⁴³

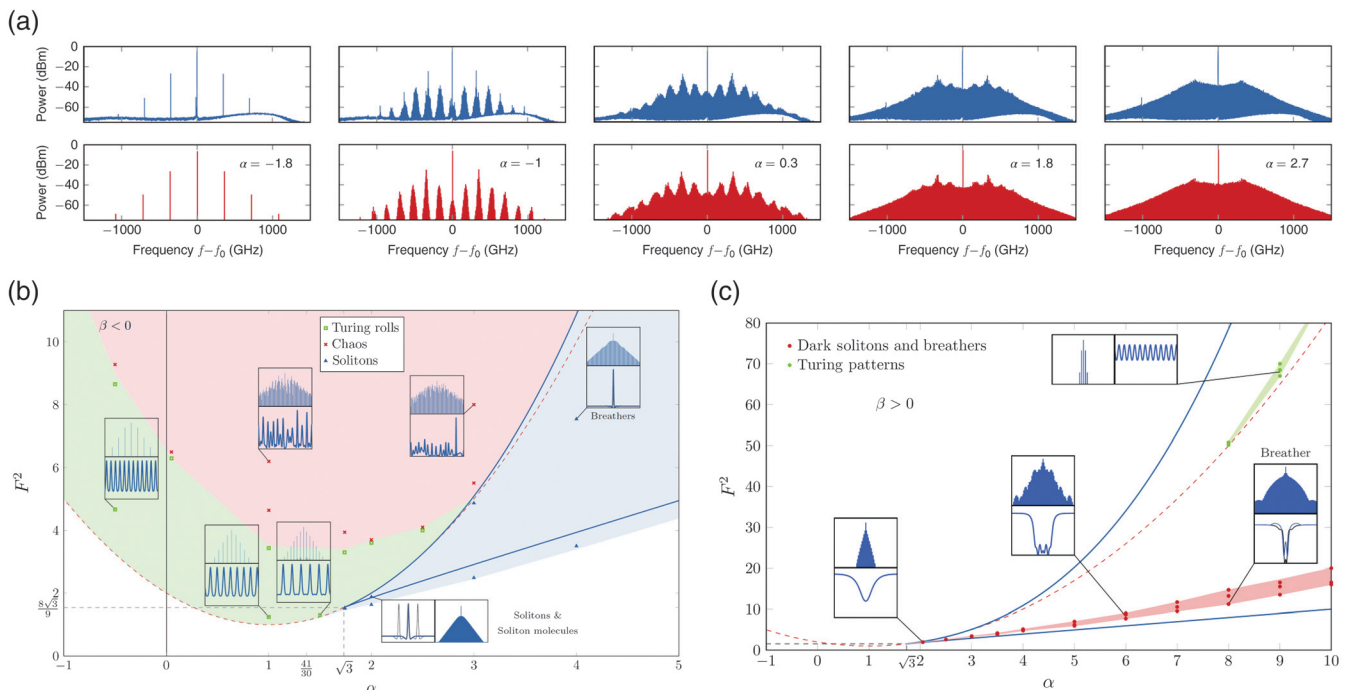


Fig. 4 Simulations and steady solutions of LLE with the corresponding experimental results. (a) Experimental (top) and simulation (bottom) results under different detuning. © 2015 John Wiley & Sons. Steady curves in the (b) anomalous and (c) normal dispersion regions. © 2014 American Physical Society (APS). Reproduced with permission.^{26,46}

method,^{25,54} a dissipated Kerr cavity soliton solution can be derived as follows:⁵⁵

$$E_{\text{cavity}} = B \operatorname{sech} \frac{\phi}{\phi_\tau} e^{i\phi} - \frac{if}{\delta\omega}, \quad (14)$$

where E_{cavity} is the overall optical field in the cavity, B is the soliton amplitude, ϕ_τ is the pulse width in the ϕ coordinate, f is the pump power, and $\delta\omega$ is the cavity-laser detuning.

Based on LLE, we can easily predict the performance of Kerr frequency comb with the dispersion management of the microresonator. Figure 4(a) depicts the simulation results of LLE, showing good agreement with the corresponding experimental results. However, even when we have the ideal dispersion curve, we still need to tune the pump laser parameters to generate the comb. Chembo et al. extensively studied the dynamic and steady states of frequency combs,^{11,28,29} presenting a concise and intuitive diagram for understanding the effect of different parameters. Figures 4(b) and 4(c) show various comb-state areas in $F^2 - \alpha$ parameter space with anomalous and normal dispersions, respectively. In the anomalous dispersion regime, for a certain pump power when the pump frequency is tuned from blue detuning to red detuning relative to the resonant frequency of the microresonator (Sec. 4.1), the states of the microresonator will change from Turing rolls to chaos and then to solitons or from Turing rolls to solitons. This theoretical prediction agrees well with the experimental results. In the normal dispersion regime, with different pump laser parameters and tuning processes, we can get the Turing patterns, breathers, and dark soliton states. Thus, we could easily obtain the tuning parameters from the diagram to achieve the desired comb states (Fig. 4).

2.3 Coupling with Other Equations

Based on the discussion of the basic governing parameters and their effects, we can have an intuitive understanding of the physical process relative to the different parameters of the microcavity-based Kerr frequency comb. To consider the effect of other parameters, such as cross modulation of different modes, second-order nonlinearity, and temperature, on the comb's evolution process, we take the turnkey soliton combs simulation¹⁷ as an example to show the detailed process. Compared with coupled mode equations that can simply add the effect terms to the equations, it is more complicated for LLE to consider other effects because of the re-derivation of LLE and coupling of LLE with other equations.

For the light coupling from the waveguide to the microresonator and back to the waveguide again, it will be ideal that light only propagate in the forward direction. However, in practice, light propagates in both clockwise and anticlockwise directions in the resonator. If an optical insulator is used in-between the microresonator and the pump laser, the back propagating wave will not affect the laser. On the other hand, the back scattering waves interfere with the generated combs, leading to more stable soliton combs. To determine the back scattering wave amplitude and feedback phase, we couple LLE with another two equations as follows:

$$\begin{aligned} \frac{\partial A_s}{\partial t} = & -\frac{\kappa}{2} A_s - i\delta\omega A_s + i\frac{D_2}{2} \frac{\partial^2 A_s}{\partial \theta^2} + i\frac{\kappa}{2} \frac{|A_s|^2 + 2|A_B|^2}{E_{\text{th}}} A_s \\ & + i\beta \frac{\kappa}{2} A_B - \sqrt{\kappa_R \kappa_L} e^{i\phi_B} A_L, \end{aligned} \quad (15)$$

$$\begin{aligned} \frac{dA_B}{dt} = & -\frac{\kappa}{2} A_B - i\delta\omega A_B + i\frac{\kappa}{2} \frac{|A_B|^2 + 2 \int_0^{2\pi} |A_s|^2 d\theta / (2\pi)}{E_{\text{th}}} A_s \\ & + i\beta \frac{\kappa}{2} \overline{A_s}, \end{aligned} \quad (16)$$

$$\begin{aligned} \frac{dA_L}{dt} = & i\delta\omega_L A_L - i\delta\omega A_L + \frac{g(|A_L^2|)}{2} (1 + i\alpha_g) A_L \\ & - \sqrt{\kappa_R \kappa_L} e^{i\phi_B} A_B. \end{aligned} \quad (17)$$

With the normalization condition and a reasonable approximation that the light traveling time in the resonator is the same as that before coupling to the resonator, Eqs. (21)–(23) can be simplified to LLE formalism as follows:

$$\begin{aligned} \frac{\partial \psi}{\partial \tau} = & -(1 + i\alpha)\psi + i\frac{D_2}{\kappa} \frac{\partial^2 \psi}{\partial \theta^2} + i(|\psi|^2 + 2|\rho_B|^2)\psi \\ & + i\beta^* \rho_B + zF, \end{aligned} \quad (18)$$

$$\frac{d\rho_B}{d\tau} = -(1 + i\alpha - 2iP - i|\rho_B|^2)\rho_B + i\beta\rho, \quad (19)$$

$$\frac{1}{iz} \frac{dz}{d\tau} = \alpha_L - \alpha + K \operatorname{Im} \left(e^{i\phi} \frac{\rho_B}{i\beta z F} \right), \quad |z| = 1, \quad (20)$$

where ψ is the normalized soliton field amplitude, ρ_B is the normalized backscattering amplitude, z is the pump phase variable, τ is the normalized evolution time, ρ is the average of ψ , and P is the total intracavity power; other parameters can be set according to the particular experiment. Equation (25) is similar to LLE and can be solved by a split-step Fourier transform as well. For more details, readers can refer to the Supplementary Material of Ref. 17.

The coupled LLEs can help us to explore the following complex phenomena in generating Kerr frequency combs: jumping in each shape spectrum induced by avoiding mode crossing,¹² spectrum broadening induced by dispersive wave,^{13,43} influence of second-order nonlinearity,⁵⁶ combs generated by cross-phase modulation (XPM),^{45,57,58} soliton crystals,^{59–63} self-injection locking.^{64,65} All these fascinating phenomena can be well explained and predicted by coupled LLEs.

3 Selection of Materials and Fabrication

To explore the rich physics and potential applications of Kerr frequency combs, they have been realized based on many different material platforms in various structures. In general, crystalline resonators made of low-index materials such as fluoride

Table 1 Different materials for generating Kerr frequency combs.

Material	Refractive index	n_2 ($\text{m}^2 \text{W}^{-1}$)	Q factor
MgF_2 ⁶⁷⁻⁶⁹	1.37	$(7-9) \times 10^{-21}$	1×10^9
CaF_2 ⁷⁰⁻⁷²	1.43	1.2×10^{-20}	1×10^{11}
BaF_2 ⁷³	1.47	2.85×10^{-20}	5×10^8
SrF_2 ⁷⁴	1.43	1.76×10^{-20}	1×10^9
Silica ^{16,66,75}	1.45	3×10^{-20}	6.7×10^8
Hydex ⁷⁶	1.7	1.15×10^{-19}	1×10^6
SiO_xN_y ⁷⁷	1.5		1.3×10^8
SiO_xC_y ^{76,78}	1.7	1.15×10^{-19}	1.2×10^6
Si_3N_4 ⁷⁹	2.0	2.5×10^{-19}	3.7×10^7
Diamond ⁸⁰	2.38	1.3×10^{-19}	1×10^6
Silicon ^{81,82}	3.47	5×10^{-18}	5.9×10^5
Ta_2O_5 ⁸³	2.05	6.2×10^{-19}	3.2×10^6
AlN ⁸⁴	2.12	2.3×10^{-19}	9.3×10^5
LiNbO_3 ⁸⁵⁻⁸⁷	2.21	1.8×10^{-19}	2.2×10^6
AlGaAs ^{88,89}	3.3	2.7×10^{-17}	1.5×10^6
GaP ⁴¹	3.05	7.8×10^{-19}	3×10^5

usually use air as cladding to confine light. Crystalline resonators are fabricated by polishing and reflow process,⁶⁶ showing Q factors as high as 10^9 (Table 1). However, crystalline resonators typically have large sizes and hence can support several modes, making the excitation of a certain mode difficult. Microdisk resonators also use air as cladding, showing Q factors as high as 10^8 . Microdisk resonators' floating structures that are fabricated by wet etching usually show poor stability.^{90,91} Furthermore, it is challenging to couple to floating structures. Compared with crystalline resonators and microdisk resonators, microring resonators can be fabricated by using a standard planar process⁹² with silicon dioxide as cladding, showing slightly lower Q factors (Table 1). Without the floating waveguide coupling, microring resonators can seamlessly couple to integrated photonics, enabling numerous applications in integrated photonics.

3.1 Potential Materials

As an ideal material to generate frequency combs, silicon nitride has a wide transparent window and anomalous dispersion regime that can be adjusted from the visible to midinfrared. Compared with other alternative materials such as lithium niobate and aluminum nitride, silicon nitride shows a more mature fabrication technique even though it does not have an electro-optic coefficient for fast soliton locking and frequency modulation. Compared with silicon oxynitride, silicon nitride has a broader transparent window, a flatter dispersion, and a larger mode volume, leading to a wider anomalous dispersion regime and a smaller size. Moreover, silicon nitride has many other attractive properties including ultrahigh hardness, excellent anti-corrosive quality, high temperature resistance, and chemical stability.

Silicon nitride was first used to achieve a low-loss waveguide in 1987⁹³ and then has been used to realize microring resonators with Q factors up to 16 million,¹⁷ leading to Kerr frequency combs. Early works focus on the high-quality thin film with

stoichiometric Si_3N_4 . Such a film is deposited by using low-pressure chemical vapor deposition (LPCVD) and has a high tensile stress exceeding 1 GPa, resulting in cracks spreading over the wafer.⁹⁴ These cracks could reduce the yield of devices drastically. Subsequently, plasma enhanced chemical vapor deposition (PECVD)⁹⁵ and silicon-rich silicon nitride⁹⁶ were used to decrease the stress. The PECVD introduces residual hydrogen, resulting in a lower Q factor. Then, crack block structure⁹⁴ and stress release structure⁹⁷ were realized. Most recently, the photonic Damascene process with preform and reflow was used to balance the stress and hence achieve crack elimination and ultrahigh Q factors simultaneously,¹⁴ paving the avenue of silicon-nitride nonlinear devices toward industry applications.

3.2 Fabrication Methods

Stoichiometric silicon nitride with a low content of hydrogen is an ideal material platform to realize octave frequency combs ranging from the visible to midinfrared.²⁰ The film is deposited in an LPCVD oven at around 800°C and 0.1 mTorr.⁹⁸ Commonly used gases are dichlorosilane and ammonia via the reaction $3\text{SiH}_2\text{Cl}_2(\text{g}) + 4\text{NH}_3(\text{g}) \rightarrow \text{Si}_3\text{N}_4(\text{s}) + 6\text{HCl}(\text{g}) + 6\text{H}_2(\text{g})$ with or without nitrogen as the carrier gas. The multiple steps of deposition can achieve a stoichiometric silicon nitride film with a thickness of around 1 μm .⁹⁸ Once the silicon-nitride film with the desired thickness is obtained, patterns can be made by spin coating, exposing, developing, etching, and finally depositing a silicon-dioxide cladding for protection (Fig. 5). During the etching process, fluorine gases are used. By adjusting the proportion of carbon, hydrogen, oxygen, and fluorine with or without a pause, which is determined by the etching rate and time, satisfactory results can be obtained. However, the etching process usually results in the periodic streaks, increasing the scattering loss and hence reducing the quality factor. Even though the reflow process is used, the stripe fluctuation still exists. In the process of the cladding deposition, bubbles may appear in the coupling gap,¹⁴ introducing a jump of the refractive index to in turn affect the coupling [Fig. 5(a)].

Subtractive process is a standard micro-nano fabrication technique. It first deposits a thick layer of Si_3N_4 on a substrate. During this deposition process, the multistep method and stress-releasing trenches are commonly used to prevent the crack generation.⁹⁴ After each deposition step, an annealing process is implemented to remove the residual hydrogen.¹⁰⁰ Then, the structures are patterned in resist and transferred to the Si_3N_4 layer by reactive ion etching (RIE). Finally, a SiO_2 cladding layer is deposited by high temperature oxide (HTO), PECVD or TEOS.^{101,102} These different processes have distinct performances in filling narrow gaps [Fig. 5(c)]. An annealing process can be used to densify the cladding layer. To obtain an ultrahigh Q factor, the subtractive process has to be optimized in the following ways. Multipass lithography,^{103,104} resist annealing,⁹⁹ and better etch recipe¹⁰⁴ can be used to reduce the sidewall roughness. Chemical mechanical polishing (CMP) can be used to acquire an ultrasurface.¹⁰⁰ To date, the subtractive process achieved a microresonator with a 3.7×10^7 Q factor for soliton generation.¹⁰⁴

The photonic Damascene process significantly increases the quality of silicon-nitride Kerr frequency combs. Damascene structures are fabricated with the reflow and CMP process to obtain an ultrasurface and surface, decreasing the

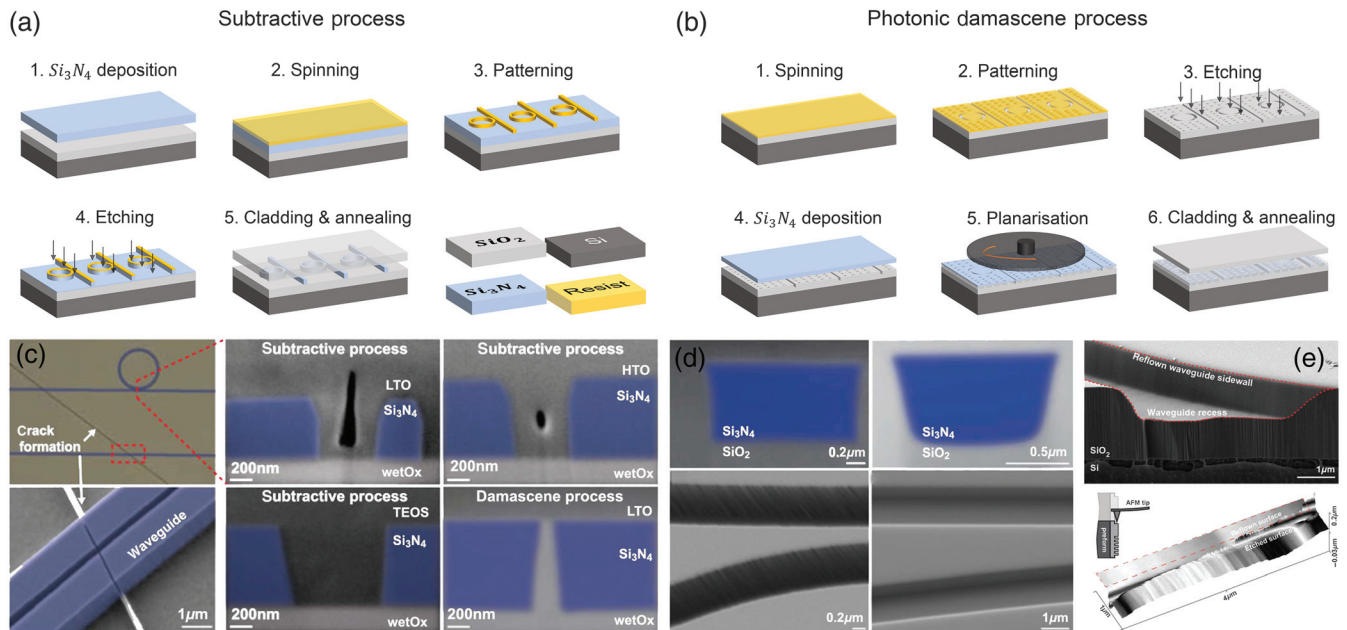


Fig. 5 Different fabrication methods for SiN microrings. (a) Subtractive process. (b) Photonic Damascene process. (c) Formation of cracks and bubbles. (d) Comparison between the devices fabricated by (a) (left) and (b) (right). © 2018 IEEE. (e) Analysis of sidewall roughness with and without the reflow technique. © 2018 Optica Publishing Group. Reproduced with permission. ^{14,99}

scattering loss and increasing the Q factor dramatically. Inspired by the additive patterning process, the Damascene process first fabricates the pattern grooves by lithography and etching, followed by the reflow process to smooth the sidewall,⁹⁹ and then deposits the stoichiometric silicon nitride to form the waveguide [Fig. 5(b)]. Distinct from depositing on flat surfaces, the top surface of the stoichiometric silicon nitride shows sags and crests with groove deposition. So, fumed SiO_2 particle slurry-based CMP is used to obtain a smooth surface. Both the subtractive and Damascene processes can acquire ultrahigh Q factors beyond 10^7 ,^{104–106} while the Damascene process can provide a better control of stress and a higher yield,¹⁰⁵ enabling various applications of silicon nitride-based Kerr frequency combs.

4 Measurement Equipment and Access to Soliton

To generate a Kerr frequency comb, we need a dynamic tuning process—adjusting the frequency of a pump laser from blue detuning to red detuning relative to the resonant frequency of the cavity in the consideration of the thermal effect.^{25,107} During the tuning process, various states will occur with different properties.^{108,109} After generating the soliton comb, the stabilization of the repetition rate and offset frequency is challenging as well. Distinct from the modulation instability (MI) combs whose comb lines' phases are unstable to each other, resulting in a high phase noise, the soliton state indicates that all the comb lines' phases vary as a function of time in the same rate, resulting in a low phase noise (Fig. 6). That is, the output of soliton state is a train of pulses; however, that of MI is not. In this section, we discuss the typical measurement setups and stabilization methods for Kerr frequency combs.

4.1 Measurement Setups

Similar to a femtosecond laser, a Kerr frequency comb in the soliton state is a train of pulses in the time domain, and a series of equally spaced spectral lines in the frequency domain. To characterize the features of Kerr frequency combs in both time domain and frequency domain, we need to conduct a series of measurements.

First, we need to measure the transmitted power by using two photodetectors and an oscilloscope. The output fiber from the microcavity connects to a power splitter whose outputs connect to a photodetector and a fiber Bragg grating to filter out the pump, respectively [Fig. 7(II)]. Hence, the variation of the total power and the power generated by nonlinear gain can be observed in the oscilloscope. When we turn the pump wavelength from wavelengths shorter than the resonance to that longer than the resonance, the output power will decrease first due to the fact that more power couples to the microcavity at the resonance. When the pump wavelength passes through the resonance peak, the output power will increase. This is a typical phenomenon in the weak pump regime.

To generate the nonlinear response, the pump must be above a threshold considering the thermal effect in the microcavity. Before the pump wavelength reaches the resonance peak, more power couples to the resonator, heating the resonator and in turn resulting in the redshift of the resonance peak. Such a regime is called thermally stable region because both the pump and resonance peak move toward longer wavelengths. In this region, MI combs and the breather state usually appear. Once the pump wavelength crosses the resonance peak, the power coupling to the resonator decreases, resulting in the cooling of the resonator and hence the blueshift of the resonant wavelength. This region is called thermally unstable region in which soliton state appears (Fig. 6). The soliton state is featured by several consecutive

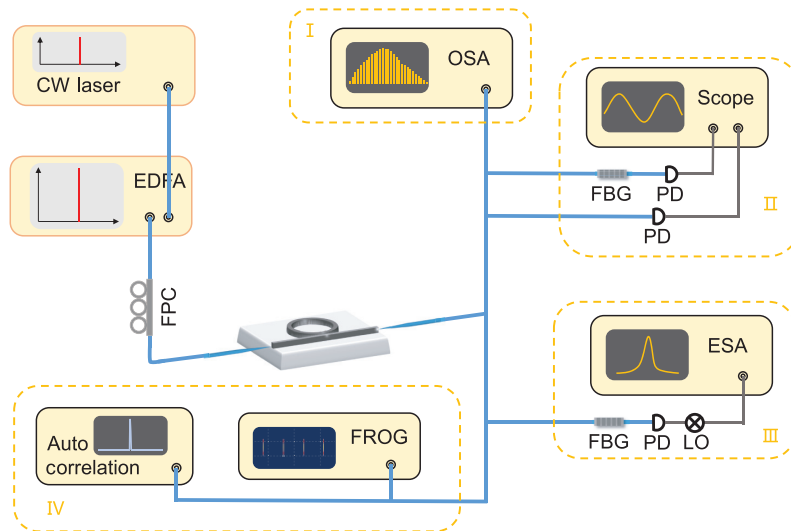


Fig. 6 Measurement setups for Kerr frequency combs. I, OSA for spectrum measurement; II, oscilloscope for transmission power monitoring; III, ESA for RF noise monitoring; IV, auto correlation or FROG for pulse measurement.

“steps” that include multi-soliton states and single soliton state. If multisoliton states appear, we can always reach a single soliton state by further tuning. However, because the pump wavelength and resonant wavelength shift in opposite directions in the thermally unstable regime, it is very challenging to reach the soliton state. In many cases, the measurement result shows the thermal triangle shape resonance peak [inset of Fig. 6(a)].

To measure the spectral features of different comb states, we can split one fiber from the output to an optical spectrum analyzer (OSA) [Fig. 7(I)]. To observe the optical phase properties, we can obtain the RF beat signal by using a local oscillator (LO) and an electrical spectrum analyzer (ESA) [Fig. 7(III)]. As shown in Fig. 6(c), in the tuning process, an MI comb appears first with a high phase noise corresponding to the random phases between different comb lines. Such a noise is chaotic along the tuning process until reaching the soliton states. In this process, the breath state may appear or not, depending on the relationship between the pump power and detuning. Further careful tuning leads to the soliton states in which the RF beat signal shows an extremely narrow bandwidth [Fig. 6(c)], indicating a tiny optical phase noise as well as stable phases of different comb lines. At

the soliton states, the output light of the microcavity is a series of femtosecond pulses. To characterize these pulses in the time domain, we need either an autocorrelation or frequency-resolved optical grating (FROG) experiment [Fig. 7(IV)]. Compared to autocorrelation, the FROG experiment can provide more information about the pulses such as the phase of the carrier wave.²⁵

By detecting in both the time and frequency domains, we can clearly observe the evolution of the comb along which the pulse width, repetition rate, and RF linewidth can be characterized for further applications. However, it is still challenging to access the soliton state via simple tuning methods.

4.2 Accessing Soliton State

Measurement of the dispersion and Q factor is necessary for comb generation. On one hand, this measurement can check the design and fabrication. On the other hand, evaluating the quality of the microresonator and searching for the tuning region are the basics for further measurement. A conventional setup is shown in Fig. 8(a). Light from the tunable continuous wave (CW) laser couples into the device. The output wave divides

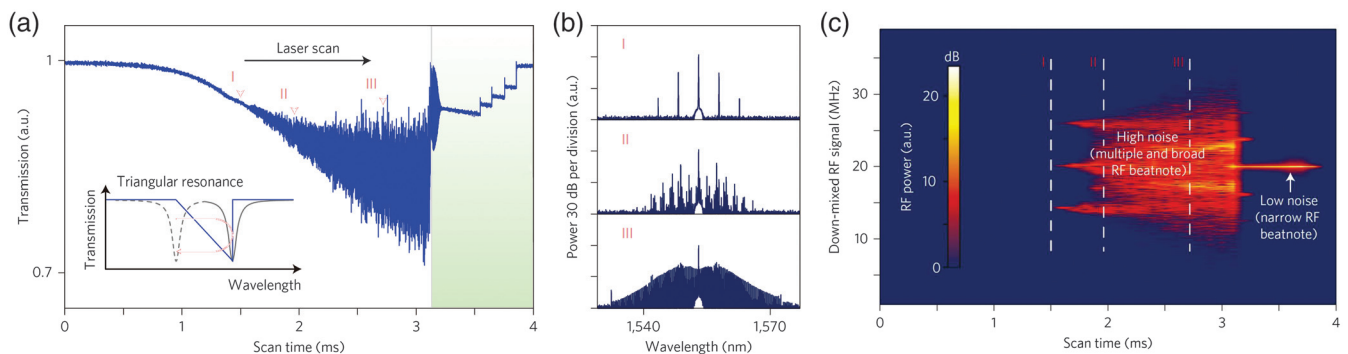


Fig. 7 Characteristics of Kerr frequency combs. (a) Transmission spectrum along the tuning of the pump laser. (b) Spectra corresponding to different regions in (a). (c) RF noise spectra corresponding to different regions in (a). © 2014 Nature Publishing Group. Reproduced with permission.²⁵

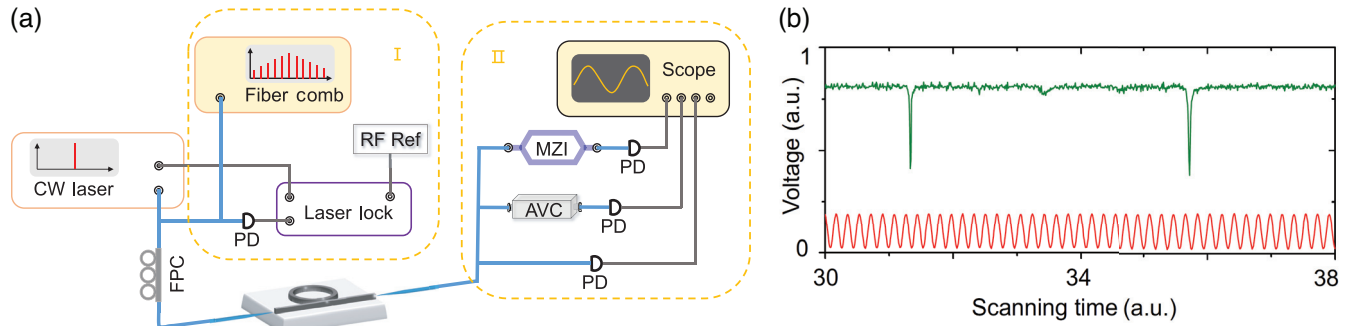


Fig. 8 Measurement of dispersion. (a) Calibration schemes based on fiber comb (I) and MZI (II). (b) Measurement results of MZI-based calibration scheme [(II) in (a)]; red line shows the MZI's interference while green line shows resonance. © 2017 Xu Yi PHD thesis. Reproduced with permission.⁵⁵

into three paths: one connects to a photodetector for monitoring the transmitted power, one connects to a Mach-Zehnder interferometer (MZI) followed by a photodetector, and the last one connects to an atomic vapor cell followed by a photodetector. The MZI is used as a ruler and the atomic vapor cell is used to calibrate the wavelength [Fig. 8(b)]. As another simpler scheme, a low repetition-rate fiber comb can be used to directly calibrate the pump laser with a high precision [Fig. 8(a)]. Such a fiber comb can measure the Q factor and dispersion that induces the nonuniform FSR. This measurement is based on the relation¹³

$$\omega_{\mu} = \omega_0 + \sum_{j=1}^{\infty} \frac{D_j \mu^j}{j!}, \quad (21)$$

where ω_0 is the resonant frequency and $\mu \in \mathbb{Z}$ is the relative mode number. $D_1/2\pi$ is the FSR and $D_2 = -(c/n)D_1^2\beta_2$ relates to the group velocity dispersion (GVD), and D_3, D_4, \dots relate to the higher-order dispersion. Conventionally, D_2 is obtained via a two-order fitting, determining the anomalous dispersion regime. Using a higher-order fitting, dispersive wave and other interesting phenomena may arise, leading to a deeper understanding and a better design.

To generate the comb after measuring the dispersion and resonant frequency, we first tune the pump laser wavelength to the expected resonant peak. Then, we increase the pump power above the threshold. Finally, we tune the laser wavelength from the blue detuning regime to the red detuning regime of the resonant peak. Due to the thermal effect, it is very challenging to access the soliton states. Many schemes have been proposed to overcome the thermal effects. One direct method is accelerating the tuning speed of the pump laser so that we can access the soliton states before the cavity cools down.^{109,110} A similar method is tuning the pump power and wavelength simultaneously.¹¹¹ Once the pump wavelength crosses the resonant wavelength, we increase the pump power to heat up the microcavity, leading to soliton states. Another method uses two pump lasers for pump and temperature control,^{16,108,112} respectively. The wavelength of one laser is tuned from blue detuning to red detuning relative to the resonant frequency while that of the auxiliary light is fixed, leading to a stationary total power in the resonator and a stable temperature. In another method, once the tuning frequency passes the resonant frequency, we can immediately tune back to shorter wavelengths,

instantaneously following the movement direction of the resonant frequency.¹¹³ The soliton states can even be accessed via thermal tuning.^{114,115} By using a temperature control circuit to control the temperature of the resonator, we can fix the pump frequency at a wavelength shorter than the resonant frequency and then blueshift the resonant frequency by thermal tuning, achieving a stable soliton state. Parametric seeding¹¹⁶ and laser self-injection locking⁶⁴ can also be used to access the soliton states. Finally, a turnkey soliton state can be achieved by taking advantage of backscattering waves¹⁷ (Sec. 2.3).

For conventional tuning methods, the key point is stabilizing the thermal effects. Furthermore, using auxiliary light along with the pump can extend the soliton step significantly,¹⁰⁸ facilitating the access of the soliton state. Moreover, in addition to the thermal stabilization, auxiliary light's different modes can also excite XPM combs whose repetition rate is the same as that of the main comb,⁴⁵ extending the comb spectrum.⁴⁵ The thermal noise has been studied in addition to controlling the thermal effects.¹¹⁷ To completely alleviate the complicated tuning process for accessing the soliton state, we will need to improve the quality of silicon-nitride film to realize an ultralow thermo-optical effect.

5 Emerging Applications in Metrology

In precision metrology, noise plays an important role because it directly determines the highest precision. For microresonator-based Kerr frequency combs, the phase noise originates from the pump laser drift, thermal effect, nonlinear effect, high-order dispersion effect, and mode crossing. MI combs featuring a high noise state are innately inappropriate for metrology, thus making the soliton state a better choice. To minimize the influence of noise, various methods are proposed. Employing an ultrastable pump laser¹⁰ and utilizing the self-injection locking mechanism^{64,65} can decrease the influence of the pump laser linewidth. Setting the laser-cavity detuning to a quiet operation point can balance the dispersive wave recoil and Raman self-frequency shift, leading to a much lower phase noise.¹¹⁸ The noise limitation of Kerr combs is determined by thermal fluctuation, relative intensity noise of pump laser, and shot noise.^{10,118}

Comb equation $f_N = f_0 + Nf_r$ shows that f_0 also plays an important role in metrology applications. Microcombs usually have a large repetition rate that is difficult to be directly detected. To detect and stabilize f_0 , the $f - 2f$ self-reference

method^{1,119,120} is used ($f_0 = 2f_N - f_{2N}$). An interlocking scheme is employed to detect the repetition rate. Furthermore, the dual comb beating method is more practical because of its simple configuration.^{2,121} In this method, two combs with a small repetition rate difference Δf_r are pumped by the same laser. The beating between those two combs can eliminate the influence of f_0 's drift and transfer f_r to Δf_r , making the signal stable and easy to be detected.

In the early stage of microcavity-based Kerr frequency combs, the community focuses on principles of generation,^{11,21–27} underlying physics,^{28,29} accessing methods,^{16,111,113,114,122} and fabrication techniques.^{14,94,97–99,123} Along the development of Kerr frequency combs,¹²⁴ the community also explores its applications including calibration of astronomical spectrographs,^{4,125} spectrum detection,^{3,126–129} ultrafast ranging with high precision,^{2,121} microwave photonics,^{130–136} terahertz generation,^{137,138} telecommunications,^{5,5,139–142} computations,¹⁴³ and quantum optics.^{144–154} In this section, we mainly discuss the applications of chip-scale Kerr frequency combs in metrology due to its significance in both fundamental science and commercial applications.

5.1 Spectral Measurement

Applications of optical frequency combs in metrology have been growing rapidly due to optical frequency combs' broad spectral range, high resolution, high sensitivity, and fast measurement speed. Among these applications, the most significant one may be dual-comb spectroscopy, which was first demonstrated in 2004.¹⁵⁵ Dual-comb spectroscopy uses two comb sources with a small difference in repetition rate Δf_r : comb 1 as the detecting source while comb 2 as a sampling source (Fig. 9). When these two light beams interfere with each other in both spatial domain and time domain, an interference pattern is generated, enabling the detection by using a regular photodetector. By detecting this interference pattern with and without the sample, we can demodulate the absorption spectrum of the sample.

In the frequency domain, the interference between the output spectra of two different combs results in an interferogram [Figs. 9(b) and 9(c)]. Such a process is also known as beating, in which two high-frequency sinusoidal waves interfere with each other, leading to a high-frequency sinusoidal wave whose amplitude is modulated by a low-frequency sinusoidal wave.

The low-frequency sinusoidal wave can be detected by the photodetector whose operating bandwidth is limited in the RF domain. That is, in the optical frequency domain, the output spectra of the two combs are

$$f_{1N} = f_0 + Nf_r, \quad (22)$$

$$f_{2N} = f_0 + N(f_r + \delta f_r). \quad (23)$$

Then the output of the photodetector (usually in the RF domain) is

$$f_N = N\delta f_r. \quad (24)$$

The RF spectrum and the comb spectrum show one-to-one correspondence. By detecting the RF spectra with and without a sample, we can obtain the absorption spectrum in the RF regime, which corresponds to the absorption spectrum in the optical regime.

Compared with Fourier transform spectrographs, dual-comb spectroscopy gets rid of a large-area beam splitter and a lift arm for scanning. Despite the compactness of chip-scale dual-comb spectrographs, a smaller comb corresponds to a larger FSR, and results in a lower resolution. This resolution can be improved by certain sampling and modulation that usually require a long measurement time. Hence, chip-scale dual comb spectrographs can be designed to either measure a certain matter by matching the comb lines with this matter's absorption peaks or achieve a high resolution by increasing the measurement time. Based on dual-comb spectroscopy, Suh et al.¹²⁶ demonstrated the detection of gas molecules by testing $\text{H}^{13}\text{CN}2\nu_3$ band. And, Ideguchi et al.³ showed that high-quality molecular spectra with a resolution below the Doppler limit can be detected by using the adaptive sample method.

5.2 Ranging and LIDAR

Frequency combs can be used for ranging via asynchronous optical sampling.¹⁵⁶ In theory, the spatial resolution δL of frequency comb-based ranging is limited by the width of the pulse (T_p). In practice, because the response time of photodetector T_{resp} is much longer than the pulse width ($T_{\text{resp}} \gg T_p$), the spatial resolution is limited by T_{resp} . Such a limitation can be

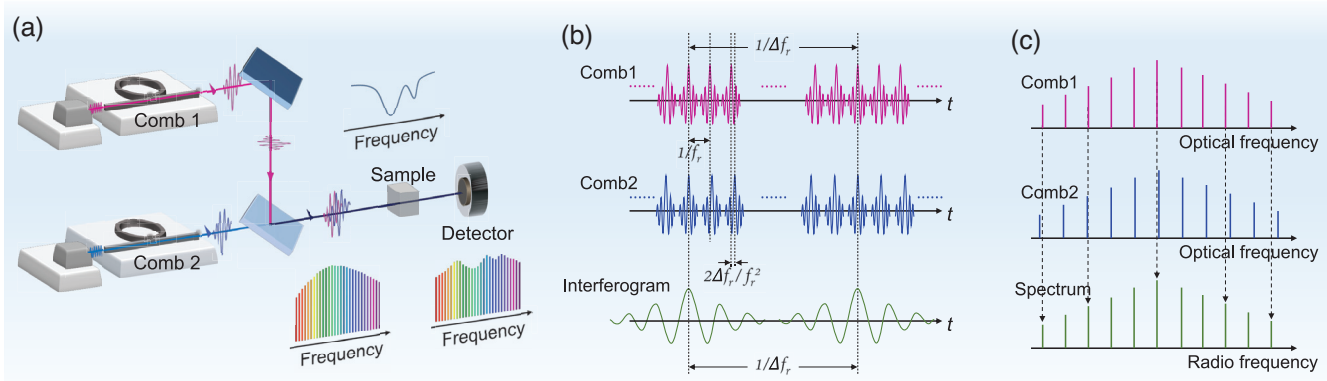


Fig. 9 Dual-comb spectroscopy. (a) Schematic of dual-comb spectroscopy. (b) Time-domain interference. (c) Beating of two frequency combs, corresponding to (b).

circumvented by dual-comb ranging, which generates an interferogram via the beating of two combs with slightly different repetition rates [Fig. 10(a)]. The interferogram's low-frequency envelope can be detected by a photodetector. The distance information can be retrieved from the low-frequency envelope — the radio-frequency comb [Fig. 10(b)]. Dual-comb ranging can achieve a 200-nm precision with chip-scale Kerr frequency combs.¹²¹ In practical applications, dual-comb ranging also needs a reference object for standardization, extraction, and postprocessing of the interferogram as well as computing the Allan deviation [Fig. 10(c)].

Recently, parallel LIDAR based on chip-scale Kerr combs achieved fast development [Fig. 10(d)]. The basic principle is frequency modulated continuous wave (FMCW). In Kerr comb generation, the single sideband modulation imposed on a pump is transferred to every comb line, leading to multiple channels

for distance and velocity measurement via FMCW [Fig. 10(d)]. Then, parallel LIDAR can be achieved by splitting the comb lines to distinct directions via a diffractive optical element.¹⁵⁷ Compared with the local oscillation signal, the corresponding received comb line shows a phase difference and a frequency shift, which can be used to retrieve the distance and velocity, respectively [Fig. 10(e)]. To simplify the detection hardware, another Kerr comb with a slightly different repetition rate can be used to achieve a multiheterodyne detection.¹⁵⁸ To increase the number of comb lines for LIDAR, a chaotic Kerr comb can be used with an auto-correlation technique.¹⁵⁹

Compared with conventional laser ranging, which measures either a relative distance with a high precision or an absolute distance with a low precision, dual-comb ranging can measure an absolute distance with a high precision. Moreover, dual-comb ranging can achieve ultrafast measurement. Recently,

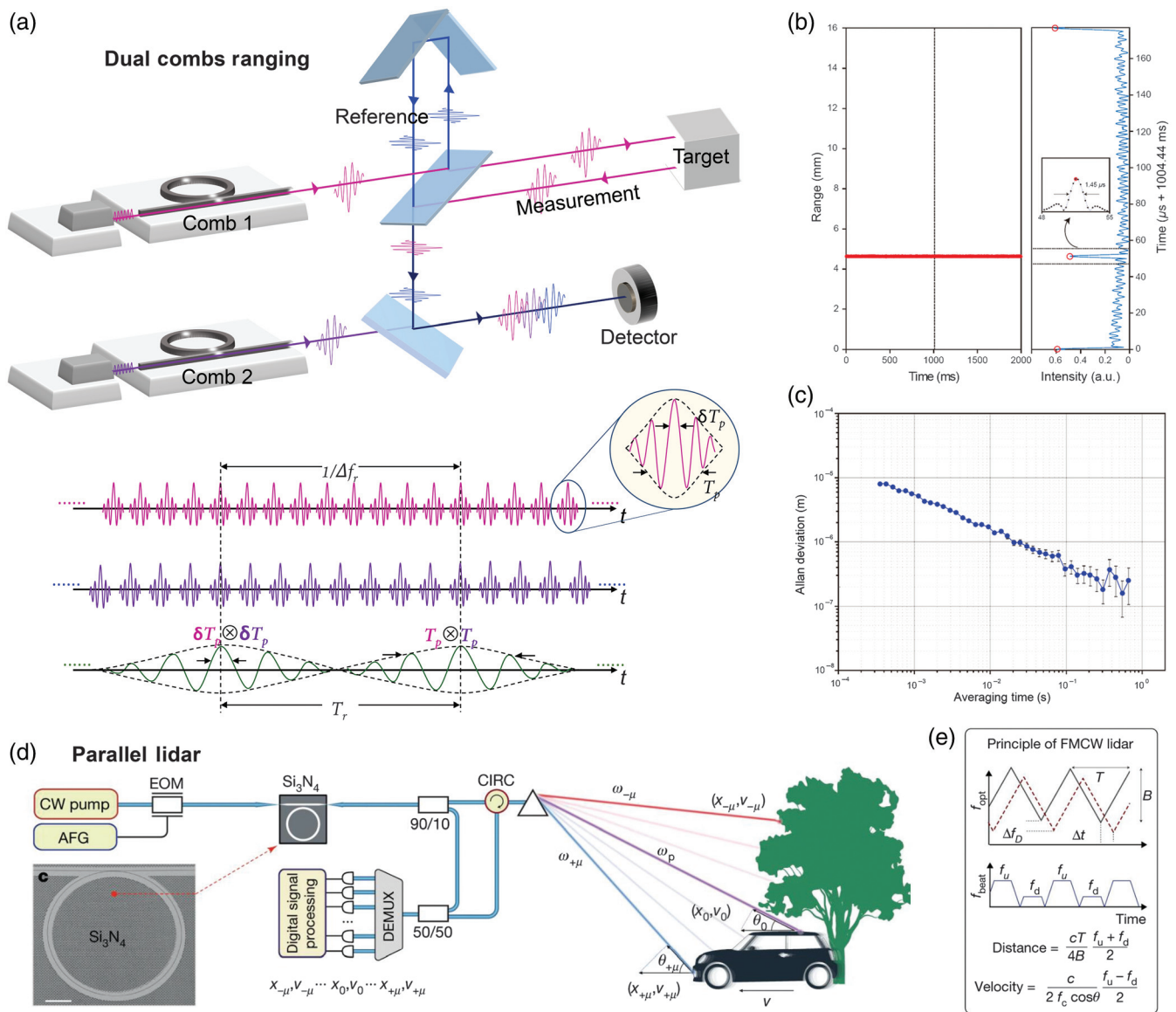


Fig. 10 Dual-comb ranging. (a) Schematic and principle of dual-comb ranging. (b) Distance measured experimentally. (c) Allan deviation of measurement. © 2018 American Association for the Advancement of Science (AAAS). (d) Schematic of parallel LIDAR. (e) Principle of FMCW. © 2020 Nature Publishing Group. Reproduced with permission.^{121,157}

Kippenberg group demonstrated a dual-comb-based ultrafast ranging with an Allan deviation down to 12 nm.² Suh et al.¹²¹ showed a time of flight measurement with 200-nm precision with dual chip-scale Kerr combs. Based on a chip-scale Kerr comb, Riemensberger et al.¹⁵⁷ achieved a frequency-modulated continuous-wave LIDAR for distance and velocity measurement at an equivalent rate of 3 megapixels per second. As chip-scale broadband highly coherent sources, Kerr frequency combs have a bright future in fast and precise ranging, as good as LIDAR, enabling applications in mechanical manufacture, autonomous vehicles, robotics, and defense industry.

5.3 Timekeeping

Considering the frequency stability of optical clocks $\frac{\delta f}{f}$, a higher transition frequency will lead to an optical clock with a higher resolution and a greater robustness against environmental noises. Compared with atomic clocks, optical clocks have been attracting extensive interest due to their ultrahigh frequency stability and relatively simple structure. Frequency combs can generate RF signals with an ultralow phase noise from optical signals via Eq. (2), enabling ultrastable optical clocks. To achieve optical clocks, a frequency comb's offset frequency needs to be locked via self-referencing, necessitating the octave frequency comb. However, it is challenging to achieve an octave frequency comb with a small FSR that can be detected by electronics. Newman et al.¹ proposed a new architecture that uses two interlocked combs with one for self-referencing and the other for generating an electronically detectable signal, realizing the 10^{-13} s short-term stability. To date, Drake et al.¹⁶⁰ have achieved a 10^{-17} absolute frequency noise based on silicon nitride microresonator.

6 Conclusion

As an ultralow phase noise, high-coherence, broadband femto-second pulse source, Kerr frequency combs dramatically boost the performance of various metrology techniques including ranging, spectroscopy, and timing. Most chip-scale Kerr frequency combs are realized based on silicon nitride due to its ultralow loss and mature craft. These combs achieve the balance between dispersion and nonlinearity under the guidance of LLE. The dynamic evolution and tuning process of combs are simulated and measured to fully understand the nonlinear interaction between light and microcavity, facilitating the access to soliton states. So far, state-of-the-art silicon nitride-based Kerr frequency combs with turnkey solitons have already been achieved in a butterfly package or heterogeneously integrated with DFB lasers.^{17,161}

For the future development of chip-scale Kerr frequency combs, LLE can be expanded to consider the effect of high-order terms of nonlinearity and dispersion. Coupled LLEs can be used to explore more complicated physics including electro-optics, acousto-optics, magneto-optics, thermo-optics and optical-optics (different modes, directions, polarizations, etc.) as well as limitations imposed by second-order nonlinearity and mode crossing. In addition to the well-developed silicon nitride, several other promising material platforms also show great potential in realizing high-performance Kerr frequency combs. Due to AlGaAs's high third-order nonlinearity, it could access the soliton state with an ultralow pump power. By taking advantage of LiNbO₃'s large electro-optic coefficient, we may achieve Kerr-frequency combs that can be tuned electrically

in an ultrafast speed.^{162,163} As the development of films with a lower thermal optical coefficient, we could discover more simple and stable tuning methods to achieve the soliton states. With the development of all these techniques, we could get turnkey solitons easily, paving the way for various applications of chip-scale Kerr frequency combs.

Acknowledgments

The authors thank Orad Reshef (the University of Ottawa), Xinyu Wang (Xi'an Institute of Optics and Precision Mechanics, Chinese Academy of Sciences), Guoqing Chang (Institute of Physics CAS), Xiaoxiao Xue (Tsinghua University), Chengying Bao (Tsinghua University) for discussions. The research described in this article was supported by the National Key Research and Development Program of China (2021YFA1401000, 2021YFB2801600, and 2017YFF0206104), National Natural Science Foundation of China (62075114 and 62175121), and the Beijing Natural Science Foundation (4212050). This work was supported by the Center of High Performance Computing, Tsinghua University.

References

1. Z. L. Newman et al., "Architecture for the photonic integration of an optical atomic clock," *Optica* **6**(5), 680–685 (2019).
2. P. Trocha et al., "Ultrafast optical ranging using microresonator soliton frequency combs," *Science* **359**(6378), 887–891 (2018).
3. T. Ideguchi et al., "Adaptive real-time dual-comb spectroscopy," *Nat. Commun.* **5**(1), 3375 (2014).
4. M.-G. Suh et al., "Searching for exoplanets using a microresonator astrocomb," *Nat. Photonics* **13**(1), 25–30 (2019).
5. P. Marin-Palomo et al., "Microresonator-based solitons for massively parallel coherent optical communications," *Nature* **546**(7657), 274–279 (2017).
6. D. T. Spencer et al., "An optical-frequency synthesizer using integrated photonics," *Nature* **557**(7703), 81–85 (2018).
7. T. Fortier and E. Baumann, "20 years of developments in optical frequency comb technology and applications," *Commun. Phys.* **2**(1), 153 (2019).
8. T. Herr et al., "Universal formation dynamics and noise of Kerr-frequency combs in microresonators," *Nat. Photonics* **6**(7), 480–487 (2012).
9. J. Li, H. Lee, and K. J. Vahala, "Microwave synthesizer using an on-chip brillouin oscillator," *Nat. Commun.* **4**(1), 2097 (2013).
10. E. Lucas et al., "Ultralow-noise photonic microwave synthesis using a soliton microcomb-based transfer oscillator," *Nat. Commun.* **11**(1), 374 (2020).
11. Y. K. Chembo and C. R. Menyuk, "Spatiotemporal Lugiato-Lefever formalism for Kerr-comb generation in whispering-gallery-mode resonators," *Phys. Rev. A* **87**(5), 053852 (2013).
12. T. Herr et al., "Mode spectrum and temporal soliton formation in optical microresonators," *Phys. Rev. Lett.* **113**(12), 123901 (2014).
13. V. Brasch et al., "Photonic chip-based optical frequency comb using soliton Cherenkov radiation," *Science* **351**(6271), 357–360 (2016).
14. M. H. P. Pfeiffer et al., "Photonic damascene process for low-loss, high-confinement silicon nitride waveguides," *IEEE J. Sel. Top. Quantum Electron.* **24**(4), 6101411 (2018).
15. J. He and Y. Li, "Design of on-chip mid-IR frequency comb with ultra-low power pump in near-IR," *Opt. Express* **28**(21), 30771–30783 (2020).
16. S. Zhang et al., "Sub-milliwatt-level microresonator solitons with extended access range using an auxiliary laser," *Optica* **6**(2), 206–212 (2019).

17. B. Shen et al., "Integrated turnkey soliton microcombs," *Nature* **582**(7812), 365–369 (2020).
18. L. A. Lugiato and R. Lefever, "Spatial dissipative structures in passive optical systems," *Phys. Rev. Lett.* **58**(21), 2209–2211 (1987).
19. P. Del'Haye et al., "Optical frequency comb generation from a monolithic microresonator," *Nature* **450**(7173), 1214–1217 (2007).
20. Q. Li et al., "Stably accessing octave-spanning microresonator frequency combs in the soliton regime," *Optica* **4**(2), 193–203 (2017).
21. M. Haelterman, S. Trillo, and S. Wabnitz, "Dissipative modulation instability in a nonlinear dispersive ring cavity," *Opt. Commun.* **91**(5–6), 401–407 (1992).
22. F. Castelli et al., "The LLE, pattern formation and a novel coherent source," *Eur. Phys. J. D* **71**(4), 84 (2017).
23. L. Maleki et al., "High performance, miniature hyper-parametric microwave photonic oscillator," in *IEEE Int. Freq. Control Symp.*, IEEE, pp. 558–563 (2010).
24. A. Matsko et al., "Mode-locked Kerr frequency combs," *Opt. Lett.* **36**(15), 2845–2847 (2011).
25. T. Herr et al., "Temporal solitons in optical microresonators," *Nat. Photonics* **8**(2), 145–152 (2014).
26. C. Godey et al., "Stability analysis of the spatiotemporal Lugiato-Lefever model for Kerr optical frequency combs in the anomalous and normal dispersion regimes," *Phys. Rev. A* **89**(6), 063814 (2014).
27. S. Coen et al., "Modeling of octave-spanning Kerr frequency combs using a generalized mean-field Lugiato–Lefever model," *Opt. Lett.* **38**(1), 37–39 (2013).
28. Y. K. Chembo, D. V. Strekalov, and N. Yu, "Spectrum and dynamics of optical frequency combs generated with monolithic whispering gallery mode resonators," *Phys. Rev. Lett.* **104**(10), 103902 (2010).
29. Y. K. Chembo and N. Yu, "Modal expansion approach to optical-frequency-comb generation with monolithic whispering-gallery-mode resonators," *Phys. Rev. A* **82**(3), 033801 (2010).
30. T. Hansson, D. Modotto, and S. Wabnitz, "On the numerical simulation of Kerr frequency combs using coupled mode equations," *Opt. Commun.* **312**, 134–136 (2014).
31. T. J. Kippenberg et al., "Dissipative Kerr solitons in optical microresonators," *Science* **361**(6402), eaan8083 (2018).
32. V. S. Ilchenko and L. Maleki, "Novel whispering-gallery resonators for lasers, modulators, and sensors," *Proc. SPIE* **4270**, 120–130 (2001).
33. A. Savchenkov et al., "Mode filtering in optical whispering gallery resonators," *Electron. Lett.* **41**(8), 495–497 (2005).
34. V. S. Ilchenko, X. S. Yao, and L. Maleki, "Microsphere integration in active and passive photonics devices," *Proc. SPIE* **3930**, 154–162 (2000).
35. S. Spillane et al., "Ideality in a fiber-taper-coupled microresonator system for application to cavity quantum electrodynamics," *Phys. Rev. Lett.* **91**(4), 043902 (2003).
36. R. Halir et al., "Ultrabroadband supercontinuum generation in a CMOS-compatible platform," *Opt. Lett.* **37**(10), 1685–1687 (2012).
37. G. Moille et al., "Broadband resonator-waveguide coupling for efficient extraction of octave-spanning microcombs," *Opt. Lett.* **44**(19), 4737–4740 (2019).
38. M. H. Pfeiffer et al., "Coupling ideality of integrated planar high- Q microresonators," *Phys. Rev. Appl.* **7**(2), 024026 (2017).
39. T. Kippenberg, S. Spillane, and K. Vahala, "Kerr-nonlinearity optical parametric oscillation in an ultrahigh- Q toroid microcavity," *Phys. Rev. Lett.* **93**(8), 083904 (2004).
40. F. Li et al., "Modeling frequency comb sources," *Nanophotonics* **5**(2), 292–315 (2016).
41. D. J. Wilson et al., "Gallium phosphide microresonator frequency combs," in *Conf. Lasers and Electro-Opt. (CLEO)*, IEEE, pp. 1–2 (2018).
42. J. Zhang et al., "Stretching the spectra of Kerr frequency combs with self-adaptive boundary silicon waveguides," *Adv. Photonics* **2**(4), 046001 (2020).
43. M. H. Pfeiffer et al., "Octave-spanning dissipative Kerr soliton frequency combs in Si_3N_4 microresonators," *Optica* **4**(7), 684–691 (2017).
44. P. Parra-Rivas et al., "Origin and stability of dark pulse Kerr combs in normal dispersion resonators," *Opt. Lett.* **41**(11), 2402–2405 (2016).
45. S. Zhang, J. Silver, and P. DelHaye, "Spectral extension and synchronization of microcombs in a single microresonator," arXiv:2002.06168 (2020).
46. P. Grelu, *Nonlinear Optical Cavity Dynamics: From Microresonators to Fiber Lasers*, John Wiley & Sons (2015).
47. J. B. Bard, "A model for generating aspects of zebra and other mammalian coat patterns," *J. Theor. Biol.* **93**(2), 363–385 (1981).
48. I. Barashenkov and Y. S. Smirnov, "Existence and stability chart for the AC-driven, damped nonlinear schrödinger solitons," *Phys. Rev. E* **54**(5), 5707–5725 (1996).
49. L. Lugiato et al., "From the Lugiato–Lefever equation to microresonator-based soliton Kerr frequency combs," *Philos. Trans. R. Soc. Am. B Math. Phys. Eng. Sci.* **376**(2135), 20180113 (2018).
50. A. Shabat and V. Zakharov, "Exact theory of two-dimensional self-focusing and one-dimensional self-modulation of waves in nonlinear media," *Sov. Phys. JETP* **34**(1), 62 (1972).
51. D. Anderson, "Variational approach to nonlinear pulse propagation in optical fibers," *Phys. Rev. A* **27**(6), 3135–3145 (1983).
52. F. G. Mertens, N. R. Quintero, and A. R. Bishop, "Nonlinear schrödinger equation with spatiotemporal perturbations," *Phys. Rev. E* **81**(1), 016608 (2010).
53. R. W. Boyd, *Nonlinear Optics*, Academic Press (2020).
54. A. B. Matsko, D. Eliyahu, and L. Maleki, "Theory of coupled optoelectronic microwave oscillator II: phase noise," *J. Opt. Soc. Am. B* **30**(12), 3316–3323 (2013).
55. X. Yi, "Physics and applications of microresonator solitons and electro-optic frequency combs," PhD thesis, California Institute of Technology (2017).
56. X. Xue, X. Zheng, and B. Zhou, "Second-harmonic induced soliton drifting and annihilation in microresonators," in *CLEO: QELS Fundam. Sci.*, Optical Society of America, p. JW2A–42 (2017).
57. C. Bao et al., "Orthogonally polarized frequency comb generation from a Kerr comb via cross-phase modulation," *Opt. Lett.* **44**(6), 1472–1475 (2019).
58. H. Wang et al., "Dirac solitons in optical microresonators," *Light Sci. Appl.* **9**(1), 205 (2020).
59. Ó. B. Helgason et al., "Dissipative solitons in photonic molecules," *Nat. Photonics* **15**(4), 305–310 (2021).
60. D. C. Cole et al., "Soliton crystals in Kerr resonators," *Nat. Photonics* **11**(10), 671–676 (2017).
61. B. Yao et al., "Gate-tunable frequency combs in graphene–nitride microresonators," *Nature* **558**(7710), 410–414 (2018).
62. M. Karpov et al., "Dynamics of soliton crystals in optical microresonators," *Nat. Phys.* **15**(10), 1071–1077 (2019).
63. Y. He et al., "Perfect soliton crystals on demand," *Laser Photonics Rev.* **14**(8), 1900339 (2020).
64. A. S. Voloshin et al., "Dynamics of soliton self-injection locking in optical microresonators," *Nat. Commun.* **12**(1), 235 (2021).
65. N. Kondratiev et al., "Self-injection locking of a laser diode to a high- Q WGM microresonator," *Opt. Express* **25**(23), 28167–28178 (2017).
66. D. Armani et al., "Ultra-high- Q toroid microcavity on a chip," *Nature* **421**(6926), 925–928 (2003).
67. I. S. Grudinin, L. Baumgartel, and N. Yu, "Frequency comb from a microresonator with engineered spectrum," *Opt. Express* **20**(6), 6604–6609 (2012).

68. N. Pavlov et al., "Narrow-linewidth lasing and soliton Kerr microcombs with ordinary laser diodes," *Nat. Photonics* **12**(11), 694–698 (2018).
69. I. S. Grudin et al., "High-contrast Kerr frequency combs," *Optica* **4**(4), 434–437 (2017).
70. I. S. Grudin, A. B. Matsko, and L. Maleki, "On the fundamental limits of Q factor of crystalline dielectric resonators," *Opt. Express* **15**(6), 3390–3395 (2007).
71. A. A. Savchenkov et al., "Kilohertz optical resonances in dielectric crystal cavities," *Phys. Rev. A* **70**(5), 051804 (2004).
72. A. A. Savchenkov et al., "Optical resonators with ten million finesse," *Opt. Express* **15**(11), 6768–6773 (2007).
73. G. Lihachev et al., "Kerr frequency comb and Brillouin lasing in BAF₂ whispering gallery mode resonator," in *Int. Conf. Laser Opt. (LO)*, IEEE, p. PD-4 (2016).
74. R. Henri et al., "Kerr optical frequency comb generation in strontium fluoride whispering-gallery mode resonators with billion quality factor," *Opt. Lett.* **40**(7), 1567–1570 (2015).
75. X. Yi et al., "Soliton frequency comb at microwave rates in a high- Q silica microresonator," *Optica* **2**(12), 1078–1085 (2015).
76. L. Razzari et al., "Cmos-compatible integrated optical hyperparametric oscillator," *Nat. Photonics* **4**(1), 41–45 (2010).
77. D. Chen et al., "On-chip ultra-high- Q silicon oxynitride optical resonators," *ACS Photonics* **4**(9), 2376–2381 (2017).
78. M. Ferrera et al., "Low-power continuous-wave nonlinear optics in doped silica glass integrated waveguide structures," *Nat. Photonics* **2**(12), 737–740 (2008).
79. Y. Okawachi et al., "Octave-spanning frequency comb generation in a silicon nitride chip," *Opt. Lett.* **36**(17), 3398–3400 (2011).
80. B. Hausmann et al., "Diamond nonlinear photonics," *Nat. Photonics* **8**(5), 369–374 (2014).
81. A. G. Griffith et al., "Silicon-chip mid-infrared frequency comb generation," *Nat. Commun.* **6**(1), 6299 (2015).
82. M. Yu et al., "Breather soliton dynamics in microresonators," *Nat. Commun.* **8**(1), 14569 (2017).
83. H. Jung et al., "Kerr solitons with tantalum ring resonators," in *Nonlinear Opt.*, Optical Society of America, p. NW2A-3 (2019).
84. H. Jung et al., "Optical frequency comb generation from aluminum nitride microring resonator," *Opt. Lett.* **38**(15), 2810–2813 (2013).
85. C. Wang et al., "Monolithic lithium niobate photonic circuits for Kerr frequency comb generation and modulation," *Nat. Commun.* **10**(1), 978 (2019).
86. Y. He et al., "Self-starting bi-chromatic LiNbO₃ soliton microcomb," *Optica* **6**(9), 1138–1144 (2019).
87. Z. Gong et al., "Soliton microcomb generation at in z-cut lithium niobate microring resonators," *Opt. Lett.* **44**(12), 3182–3185 (2019).
88. M. Pu et al., "Efficient frequency comb generation in AlGaAs-on-insulator," *Optica* **3**(8), 823–826 (2016).
89. L. Chang et al., "Ultra-efficient frequency comb generation in AlGaAs-on-insulator microresonators," *Nat. Commun.* **11**(1), 1331 (2020).
90. K. Y. Yang et al., "Ultra-high- Q silica-on-silicon ridge-ring-resonator with an integrated silicon nitride waveguide," in *CLEO: QELS_Fundam. Sci.*, Optical Society of America, p. JTh4B-7 (2016).
91. J.-F. Ku et al., "Whispering-gallery-mode microdisk lasers produced by femtosecond laser direct writing," *Opt. Lett.* **36**(15), 2871–2873 (2011).
92. A. Rahim et al., "Expanding the silicon photonics portfolio with silicon nitride photonic integrated circuits," *J. Lightwave Technol.* **35**(4), 639–649 (2017).
93. C. H. Henry et al., "Low loss Si₃N₄-SiO₂ optical waveguides on Si," *Appl. Opt.* **26**(13), 2621–2624 (1987).
94. K. Luke et al., "Overcoming Si₃N₄ film stress limitations for high quality factor ring resonators," *Opt. Express* **21**(19), 22829–22833 (2013).
95. C. J. Krückel et al., "Linear and nonlinear characterization of low-stress high-confinement silicon-rich nitride waveguides," *Opt. Express* **23**(20), 25827–25837 (2015).
96. K. Ooi et al., "Pushing the limits of cmos optical parametric amplifiers with usrn: Si₇N₄ above the two-photon absorption edge," *Nat. Commun.* **8**(1), 13878 (2017).
97. M. H. Pfeiffer et al., "Photonic damascene process for integrated high- Q microresonator based nonlinear photonics," *Optica* **3**(1), 20–25 (2016).
98. A. Gondarenko, J. S. Levy, and M. Lipson, "High confinement micron-scale silicon nitride high Q ring resonator," *Opt. Express* **17**(14), 11366–11370 (2009).
99. M. H. Pfeiffer et al., "Ultra-smooth silicon nitride waveguides based on the damascene reflow process: fabrication and loss origins," *Optica* **5**(7), 884–892 (2018).
100. X. Ji et al., "Methods to achieve ultra-high quality factor silicon nitride resonators," *APL Photonics* **6**(7), 071101 (2021).
101. Z. Ye et al., "High- Q Si₃N₄ microresonators based on a subtractive processing for Kerr nonlinear optics," *Opt. Express* **27**(24), 35719–35727 (2019).
102. M. W. Puckett et al., "422 million intrinsic quality factor planar integrated all-waveguide resonator with sub-MHz linewidth," *Nat. Commun.* **12**(1), 934 (2021).
103. R. J. Bojko et al., "Electron beam lithography writing strategies for low loss, high confinement silicon optical waveguides," *J. Vac. Sci. Technol. B* **29**(6), 06F309 (2011).
104. X. Ji et al., "Ultra-low-loss on-chip resonators with sub-milliwatt parametric oscillation threshold," *Optica* **4**(6), 619–624 (2017).
105. J. Liu et al., "High-yield, wafer-scale fabrication of ultralow-loss, dispersion-engineered silicon nitride photonic circuits," *Nat. Commun.* **12**(1), 2236 (2021).
106. H. El Dirani et al., "Ultralow-loss tightly confining Si₃N₄ waveguides and high- Q microresonators," *Opt. Express* **27**(21), 30726–30740 (2019).
107. Y. Li et al., "Real-time transition dynamics and stability of chip-scale dispersion-managed frequency microcombs," *Light Sci. Appl.* **9**(1), 52 (2020).
108. W. Wang, L. Wang, and W. Zhang, "Advances in soliton microcomb generation," *Adv. Photonics* **2**(3), 034001 (2020).
109. D. C. Cole et al., "Kerr-microresonator solitons from a chirped background," *Optica* **5**(10), 1304–1310 (2018).
110. T. C. Briles et al., "Interlocking Kerr-microresonator frequency combs for microwave to optical synthesis," *Opt. Lett.* **43**(12), 2933–2936 (2018).
111. V. Brasch et al., "Bringing short-lived dissipative Kerr soliton states in microresonators into a steady state," *Opt. Express* **24**(25), 29312–29320 (2016).
112. H. Zhou et al., "Soliton bursts and deterministic dissipative Kerr soliton generation in auxiliary-assisted microcavities," *Light Sci. Appl.* **8**(1), 50 (2019).
113. H. Guo et al., "Universal dynamics and deterministic switching of dissipative Kerr solitons in optical microresonators," *Nat. Phys.* **13**(1), 94–102 (2017).
114. C. Joshi et al., "Thermally controlled comb generation and soliton modelocking in microresonators," *Opt. Lett.* **41**(11), 2565–2568 (2016).
115. Z. Lu et al., "Deterministic generation and switching of dissipative Kerr soliton in a thermally controlled micro-resonator," *AIP Adv.* **9**(2), 025314 (2019).
116. J. Wang et al., "Deterministic single soliton formation and manipulation in anomalous dispersion microresonators via parametric seeding," *IEEE Photonics J.* **10**(3), 6100608 (2018).
117. T. E. Drake et al., "Thermal decoherence and laser cooling of Kerr microresonator solitons," *Nat. Photonics* **14**(8), 480–485 (2020).
118. X. Yi et al., "Single-mode dispersive waves and soliton microcomb dynamics," *Nat. Commun.* **8**(1), 14869 (2017).

119. J. D. Jost et al., "Counting the cycles of light using a self-referenced optical microresonator," *Optica* **2**(8), 706–711 (2015).
120. P. Del'Haye et al., "Phase-coherent microwave-to-optical link with a self-referenced microcomb," *Nat. Photonics* **10**(8), 516–520 (2016).
121. M.-G. Suh and K. J. Vahala, "Soliton microcomb range measurement," *Science* **359**(6378), 884–887 (2018).
122. T. Wildi et al., "Thermally stable access to microresonator solitons via slow pump modulation," *Opt. Lett.* **44**(18), 4447–4450 (2019).
123. K. H. Nam, I. H. Park, and S. H. Ko, "Patterning by controlled cracking," *Nature* **485**(7397), 221–224 (2012).
124. B. Stern et al., "Battery-operated integrated frequency comb generator," *Nature* **562**(7727), 401–405 (2018).
125. E. Ozbud et al., "A microphotonic astrocomb," *Nat. Photonics* **13**(1), 31–35 (2019).
126. M.-G. Suh et al., "Microresonator soliton dual-comb spectroscopy," *Science* **354**(6312), 600–603 (2016).
127. C. Gu et al., "Passive coherent dual-comb spectroscopy based on optical-optical modulation with free running lasers," *Photonix* **1**(1), 7 (2020).
128. Y. Wang et al., "Scanning dual-microcomb spectroscopy," *Sci. China Phys. Mech. Astron.* **65**(9), 294211 (2022).
129. C. Bao et al., "Architecture for microcomb-based GHz-mid-infrared dual-comb spectroscopy," *Nat. Commun.* **12**(1), 6573 (2021).
130. J. Wu et al., "RF photonics: an optical microcombs' perspective," *IEEE J. Sel. Top. Quantum Electron.* **24**(4), 6101020 (2018).
131. X. Xue et al., "Programmable single-bandpass photonic RF filter based on Kerr comb from a microring," *J. Lightwave Technol.* **32**(20), 3557–3565 (2014).
132. T. G. Nguyen et al., "Integrated frequency comb source based Hilbert transformer for wideband microwave photonic phase analysis," *Opt. Express* **23**(17), 22087–22097 (2015).
133. X. Xu et al., "Reconfigurable broadband microwave photonic intensity differentiator based on an integrated optical frequency comb source," *APL Photonics* **2**(9), 096104 (2017).
134. X. Xu et al., "Advanced RF and microwave functions based on an integrated optical frequency comb source," *Opt. Express* **26**(3), 2569–2583 (2018).
135. F. Ferdous et al., "Spectral line-by-line pulse shaping of on-chip microresonator frequency combs," *Nat. Photonics* **5**(12), 770–776 (2011).
136. X. Xue et al., "Microresonator frequency combs for integrated microwave photonics," *IEEE Photonics Technol. Lett.* **30**(21), 1814–1817 (2018).
137. T. Yasui et al., "Terahertz frequency metrology based on frequency comb," *IEEE J. Sel. Top. Quantum Electron.* **17**(1), 191–201 (2010).
138. S. Zhang et al., "Terahertz wave generation using a soliton microcomb," *Opt. Express* **27**(24), 35257–35266 (2019).
139. A. Fülöp et al., "Long-haul coherent communications using microresonator-based frequency combs," *Opt. Express* **25**(22), 26678–26688 (2017).
140. J. Pfeifle et al., "Coherent terabit communications with microresonator Kerr frequency combs," *Nat. Photonics* **8**(5), 375–380 (2014).
141. H. Shu et al., "Microcomb-driven silicon photonic systems," *Nature* **605**(7910), 457–463 (2022).
142. A. Fülöp et al., "High-order coherent communications using mode-locked dark-pulse Kerr combs from microresonators," *Nat. Commun.* **9**(1), 1598 (2018).
143. J. Feldmann et al., "Parallel convolutional processing using an integrated photonic tensor core," *Nature* **589**(7840), 52–58 (2021).
144. C. Reimer et al., "Integrated frequency comb source of heralded single photons," *Opt. Express* **22**(6), 6535–6546 (2014).
145. N. C. Menicucci, S. T. Flammia, and O. Pfister, "One-way quantum computing in the optical frequency comb," *Phys. Rev. Lett.* **101**(13), 130501 (2008).
146. M. Kues et al., "Quantum optical microcombs," *Nat. Photonics* **13**(3), 170–179 (2019).
147. C. Reimer et al., "Generation of multiphoton entangled quantum states by means of integrated frequency combs," *Science* **351**(6278), 1176–1180 (2016).
148. M. Kues et al., "On-chip generation of high-dimensional entangled quantum states and their coherent control," *Nature* **546**(7660), 622–626 (2017).
149. F.-X. Wang et al., "Quantum key distribution with on-chip dissipative Kerr soliton," *Laser Photonics Rev.* **14**(2), 1900190 (2020).
150. L. Caspani et al., "Multifrequency sources of quantum correlated photon pairs on-chip: a path toward integrated quantum frequency combs," *Nanophotonics* **5**(2), 351–362 (2016).
151. C. Xiong, B. Bell, and B. J. Eggleton, "CMOS-compatible photonic devices for single-photon generation," *Nanophotonics* **5**(3), 427–439 (2016).
152. R. Wakabayashi et al., "Time-bin entangled photon pair generation from Si micro-ring resonator," *Opt. Express* **23**(2), 1103–1113 (2015).
153. D. Grassani et al., "Micrometer-scale integrated silicon source of time-energy entangled photons," *Optica* **2**(2), 88–94 (2015).
154. P. Imany et al., "50-GHz-spaced comb of high-dimensional frequency-bin entangled photons from an on-chip silicon nitride microresonator," *Opt. Express* **26**(2), 1825–1840 (2018).
155. F. Keilmann, C. Gohle, and R. Holzwarth, "Time-domain mid-infrared frequency-comb spectrometer," *Opt. Lett.* **29**(13), 1542–1544 (2004).
156. H. Zhang et al., "Absolute distance measurement by dual-comb nonlinear asynchronous optical sampling," *Opt. Express* **22**(6), 6597–6604 (2014).
157. J. Riemensberger et al., "Massively parallel coherent laser ranging using a soliton microcomb," *Nature* **581**(7807), 164–170 (2020).
158. A. Lukashchuk et al., "Dual chirped microcomb based parallel ranging at megapixel-line rates," *Nat. Commun.* **13**(1), 3280 (2022).
159. A. Lukashchuk et al., "Chaotic micro-comb based parallel ranging," arXiv:2112.10241 (2021).
160. T. E. Drake et al., "Terahertz-rate Kerr-microresonator optical clockwork," *Phys. Rev. X* **9**(3), 031023 (2019).
161. C. Xiang et al., "Laser soliton microcombs heterogeneously integrated on silicon," *Science* **373**(6550), 99–103 (2021).
162. M. G. Vazimali and S. Fathpour, "Applications of thin-film lithium niobate in nonlinear integrated photonics," *Adv. Photonics* **4**(3), 034001 (2022).
163. G. Chen et al., "Advances in lithium niobate photonics: development status and perspectives," *Adv. Photonics* **4**(3), 034003 (2022).

Zhaoyang Sun received his BS degree in physics from Jilin University, China, in 2018. Currently, he is pursuing a PhD in optical engineering at Tsinghua University. His research interests are in micro-nano fabrication and photonics integrated circuits. He is a member of COS.

Yang Li received his BS degree in telecommunication engineering in 2006 and his MS degree in electromagnetic field and microwave technology in 2008 from Huazhong University of Science and Technology, China, and his PhD in electrical engineering from Iowa State University in 2012. His research interests include integrated metamaterials and integrated lithium-niobate photonics. He is a member of IEEE, OSA, SPIE, COS, and CSOE.

Benfeng Bai received his BSc and PhD degrees in optical engineering from Tsinghua University, China, in 2001 and 2006, respectively. Now, he is an associate professor in the Department of Precision Instrument, Tsinghua University. His research interests are in nanophotonics and near-field optics. He is a member of the National Nanotechnology Standardization Committee of China and of IEEE, OSA, SPIE, and COS.

Zhendong Zhu received his BSc and MS degrees in materials science and engineering, Sichuan University, China, in 2001 and 2005, respectively, and his PhD in optical engineering from Tsinghua University, China, in 2015. His research interests are on nanophotonics and photonic integrated circuits. He is a member of the National Nanotechnology Standardization Committee of China.

Hongbo Sun received his BS and PhD degrees in electronics from Jilin University, China, in 1992 and 1996, respectively. In 2004, he was promoted as a full professor (Changjiang Scholar) at Jilin University. Since 2017, he has been working at Tsinghua University, China. His research interests are in ultrafast and nanophotonics. He is an IEEE, OSA, SPIE, and COS fellow.